

Requirements for Making Thick Junctions of Organic Solar Cells based on Nonfullerene Acceptors

Mathias Nyman,* Oskar J. Sandberg,* Wei Li, Stefan Zeiske, Robin Kerremans, Paul Meredith, and Ardalan Armin*

Organic bulk-heterojunction solar cells based on the newly developed nonfullerene electron acceptors have the potential for very low-cost energy production. However, to enable large-scale production with common printing techniques, the active layer thicknesses need to be increased by up to an order of magnitude, which is currently not possible without significant loss in performance. Herein, the requirements for making nonfullerene acceptor (NFA)-based solar cells with thick active layers and high efficiencies are clarified. The charge carrier mobility, unintentional doping concentrations, and bimolecular recombination prefactor in the model high-efficiency system PM6 (Poly[(2,6-(4,8-bis(5-(2-ethylhexyl-3-fluoro)thiophen-2-yl)-benzo[1,2-*b*:4,5-*b'*]dithiophene))-*alt*-(5,5-(1',3'-di-2-thienyl-5',7'-bis(2-ethylhexyl)benzo[1',2'-*c*:4',5'-*c'*]dithiophene-4,8-dione))]:Y6 (2,2'-((2*Z*,2'*Z*)-((12,13-bis(2-ethylhexyl)-3,9-diundecyl-12,13-dihydro-[1,2,5]thiadiazolo[3,4-*e*]thieno[2'',3'':4',5']thieno[2',3':4,5]pyrrolo[3,2-*g*]thieno[2',3':4,5]thieno[3,2-*b*]indole-2,10-diyl)bis(methanylylidene))bis(5,6-difluoro-3-oxo-2,3-dihydro-1*H*-indene-2,1-diylidene))dimalononitrile) are determined. The results are implemented in a combined electro-optical device model, which is used to determine the effect of varying these parameters on the efficiency. The results show that a mobility imbalance and doping can lead to improved performance at large thicknesses, partially contradicting previous studies performed on fullerene-based systems. The findings highlight the importance of determining electron and hole mobilities selectively, as well as characterizing recombination and doping concentrations.


1. Introduction

Solar cells based on solution processable organic semiconductors hold great potential for future small- and large-scale energy production and could dramatically expand the range of applications for which photovoltaics are suited. In recent years, the field has seen significant advances mostly due to the success of various newly developed nonfullerene acceptors (NFAs),^[1] with power conversion efficiencies (PCEs) currently exceeding 18%.^[2] Although these NFAs are superior to the historically dominant fullerenes in many respects, such as high exciton separation efficiency at low driving energies, traditional fullerenes are still superior to many NFAs in terms of charge transport and collection.^[1,3–5] Because of impaired extraction efficiency, the champion NFA-based devices in many cases have active layers (junctions) less than 100 nm thick, and the PCE can be quite sensitive to thickness variations (notable exceptions will be discussed later). In thicker layers, primarily the fill factor (FF) is reduced, but typically also the short circuit current (J_{SC}).^[6,7]

Large area printing techniques are not compatible with manufacturing devices with active layer thicknesses of 100 nm or less—yields are low and defect densities are high. To utilize fully the potential of solution processable materials, the active layer thicknesses need to be increased, preferably up to 500 nm or more without significant loss in performance.^[8] For this to be possible, the properties of the bulk active layer need to meet a number of criteria, based on information in the literature. First, it has been argued that the charge carrier mobilities of electrons and holes should be high (preferably $>10^{-3} \text{ cm}^2 \text{ Vs}^{-1}$) and more preferably balanced as unbalanced mobilities can lead to space-charge effects reducing the FF.^[7–10] Currently, the charge carrier mobility in bulk heterojunctions (BHJ) at carrier densities relevant for operating conditions is in many cases limited to of order $10^{-4} \text{ cm}^2 \text{ Vs}^{-1}$ or less. In fullerene-based systems the electron mobility is typically higher than the hole mobility, whereas in NFA-based systems the opposite is more common—mobility imbalances of one order of magnitude or more are not uncommon. In devices with thin active layers ($<100 \text{ nm}$), this is rarely a problem. However, issues arise

Dr. M. Nyman
Physics, Faculty of Science and Engineering
Åbo Akademi University
Porthansgatan 3, 20500 Turku, Finland
E-mail: mathnyma@abo.fi

Dr. O. J. Sandberg, Dr. W. Li, S. Zeiske, R. Kerremans, Prof. P. Meredith, Dr. A. Armin
Sustainable Advanced Materials (Sêr SAM)
Department of Physics
Swansea University
Singleton Park, Swansea SA2 8PP, UK
E-mail: o.j.sandberg@swansea.ac.uk; ardalan.armin@swansea.ac.uk

 The ORCID identification number(s) for the author(s) of this article can be found under <https://doi.org/10.1002/solr.202100018>.

© 2021 The Authors. Solar RRL published by Wiley-VCH GmbH. This is an open access article under the terms of the Creative Commons Attribution License, which permits use, distribution and reproduction in any medium, provided the original work is properly cited.

DOI: 10.1002/solr.202100018

when the device active layer thickness becomes large enough so that the slower charge carrier forms a space charge region screening the internal electric field resulting in a lower FF. In the very thick junctions imbalanced charge carrier extraction may also result in charge collection narrowing (CCN), i.e., the internal quantum efficiency being suppressed at photon energies above the optical gap. CCN is detrimental to the solar cell efficiency via lowering the photocurrent, however, it has been shown useful in narrowband photodetectors.^[11]

Second, conventional wisdom dictates that the active layer should be undoped to avoid the formation of a depletion region, which could negatively affect the FF.^[12] Unintentional doping concentrations on the order of 10^{15} – 10^{16} cm⁻³ in nominally intrinsic absorber layers have been reported in several systems.^[13–18] As in the case of unbalanced mobilities, doping concentrations on the order of 10^{16} cm⁻³ are unlikely to have a very large effect on thin devices (<100 nm) since the active layer would normally be fully depleted by the built-in voltage at short circuit. A negative effect on the FF is seen when the depletion region at short circuit becomes smaller than the active layer thickness. In this case, charges are efficiently extracted only in the depletion region, whereas charges generated in the neutral region will recombine (unless recombination is significantly reduced compared with the Langevin limit). As the depletion region width is voltage dependent, this will lead to a voltage-dependent photocurrent.^[12]

Third, the bulk recombination coefficient β should be significantly reduced compared to the Langevin recombination coefficient β_L given by: $\beta_L = q \frac{\mu_n + \mu_p}{\epsilon \epsilon_0}$ where q = elementary charge, μ_n = electron mobility, μ_p = hole mobility, ϵ = relative permittivity, and ϵ_0 = the vacuum permittivity.^[8] There are several fullerene-based systems with significantly reduced bimolecular recombination,^[19–22] most notably BQR:PC₇₀BM which has a bimolecular recombination coefficient that is ≈ 2000 times reduced compared with Langevin.^[22] However, fullerene-based systems are not technologically relevant mainly due to lower efficiencies and less stable morphology compared with NFA-based systems; the morphology of fullerene-based systems is not quenched, i.e., solvent annealing or similar is often needed to acquire the optimum morphology. Recently, a number of NFA-based systems have been reported to perform well even in thick junctions.^[23–27] In particular, the PM6:Y6 blend is a promising candidate for making thick devices.^[23–25]

New NFAs as well as polymer donors are being developed at an unprecedented rate, which has led to several record breaking BHJ solar cells being reported over the last few years. However, the charge transport and nongeminate recombination in these materials—critical properties to understand for scaling to technologically meaningful cell areas, are often not comprehensively characterized.^[8] All methods have their advantages and drawbacks, and given the complexity of (nonequilibrium) charge transport in disordered systems,^[28] several techniques in combination with modeling is needed for a comprehensive picture. In this article, we clarify the requirements for making NFA-based solar cells with thick active layers. We determine the charge carrier mobility, unintentional doping concentrations and bimolecular recombination prefactor in the model system PM6:Y6 using several techniques. These results are used as input parameters in

a combined electro-optical model, which we use to simulate J – V characteristics of devices with varying thicknesses. The simulated J – V curves are compared with experimentally determined ones. We furthermore vary the charge carrier mobilities, doping concentrations and bimolecular recombination prefactors in our simulations, to outline design principles for making NFA-based solar cells with thick active layers.

2. Results and Discussion

Charge carrier mobilities were determined using Resistance-dependent photovoltage (RPV),^[29] metal–insulator–metal charge extraction by a linearly increasing voltage (MIM-CELIV)^[30,31] and metal–insulator–semiconductor charge extraction by a linearly increasing voltage (MIS-CELIV).^[32,33] RPV and MIM-CELIV were carried out on PM6:Y6 solar cells with inverted device structures (glass/ITO/ZnO/active layer/MoO₃/Ag). RPV can be used to selectively measure the mobility of the two different photogenerated charge carrier types provided that the mobilities are sufficiently imbalanced, whereas MIM-CELIV measures the mobility of the more conductive charge carrier. In addition, MIS-CELIV was carried out on hole-only and electron-only metal–insulator–semiconductor (MIS) devices to selectively measure the mobility of injected electrons and holes. All techniques give similar results; RPV shows balanced mobilities around 2×10^{-4} cm² Vs⁻¹, whereas the ambipolar mobility as determined from MIM-CELIV is 1.4×10^{-4} cm² Vs⁻¹. MIS-CELIV gives an electron mobility of 4×10^{-4} cm² Vs⁻¹ and hole mobility of 1.4×10^{-4} cm² Vs⁻¹. The extraction current transients are provided in the Figure S1–S3, Supporting Information. We note that a mobility imbalance of a factor of three seen in the MIS-CELIV measurements are probably not resolvable in RPV explaining why only one transit time is observed in RPV (Figure S1, Supporting Information). In addition, the error in the mobility determination is typically up to a factor of two with these techniques^[31]; it is therefore possible that the mobility imbalance is significantly larger, or indeed smaller.

Furthermore, dark CELIV carried out on both a 700 nm thick inverted solar cell (SC), and a 350 nm MIS device revealed both to be unintentionally doped.^[34,35] Based on conducting CELIV in the capacitive regime (doping-CELIV), the doping concentrations were determined to be 3.3×10^{15} cm⁻³ and 6.5×10^{15} cm⁻³ in the SC device and MIS device, respectively; the extraction current transients with varying voltage ramp rates are shown in Figure S4, Supporting Information. The source of this unintentional doping is not clear, there are several possibilities reported in the literature such as oxidization in the presence of water or oxygen, diffusion from contacts and residue from synthesis. However, given that similar doping concentrations are seen in devices with completely different contacts, it is unlikely that diffusion from the contacts is the only source. We further note that an increase in the doping concentration was seen after leaving the devices in air overnight suggesting oxidization could account for at least some of the doping sources. Oxidization typically leads to p -doping, however, at this stage, it is not possible to know for certain whether the devices are p - or n -doped.

The bimolecular recombination reduction factor $\zeta = \beta_L/\beta$ was determined using the double-injection (DoI) technique.^[36–38] In

DoI, a voltage (either pulsed or steady state) is applied in the forward bias of a diode with ohmic contacts whereby electrons are injected at the cathode and holes at the anode. At a large enough forward-bias voltage, the current will be limited by the recombination in the bulk. Provided that the electron and hole mobilities are known, the reduction factor can be determined. Details of the technique can be found in Experimental Section. Figure S5, Supporting Information, shows the DoI current as a function of voltage for an inverted SC device. As shown in Figure S5, Supporting Information, the experimentally obtained current and the analytical expression are in good agreement. In addition, the numerical drift–diffusion (DD) simulations describe the voltage-dependent behavior of the photocurrent (even at lower voltages) very well. The reduction factor is determined to be $\zeta \approx 400$. We note that some metal oxides are prone to a light soaking effect,^[39] however, a 10 min light soak under artificial sunlight (AM1.5) did not cause any significant change in the DoI currents in our case indicating that the ZnO that was used is relatively stable.

In **Figure 1a**, the absorption coefficient as a function of wavelength of a PM6:Y6 blend (donor–acceptor ratio 1:1.2) is shown, the absorption coefficients for PCDTBT:PC₇₀BM (donor–acceptor ratio 1:1) and P3HT:PC₆₀BM (donor–acceptor ratio 1:1) are shown for comparison. The PM6:Y6 spectrum shows very efficient absorption over the whole range between 400 and 900 nm, as compared with the P3HT:PC₆₀BM and PCDTBT:PC₇₀BM spectra, which do not absorb significantly above 700 nm and have lower overall absorption coefficients. This is typical for NFA-based blends as NFAs absorb light more efficiently in the visible range than do fullerene-based ones—a feature referred to as complementary absorption. This fact leads to a spatially more confined absorption profile within thicker active layer; i.e., most of the absorption occurs closer to the transparent contact in NFA-based systems than in fullerene-based systems. This is illustrated in **Figure 1b** which shows the generation rate profile for charge carriers inside the active layer for PM6:Y6 calculated using an optical transfer-matrix model.^[40,41] For the thick 500 nm case, most of the light is absorbed within the first 100 nm from the transparent contact.

The results presented earlier were implemented in an electro-optical 1D DD model,^[42] used to determine the effect of varying

charge carrier mobility, doping concentrations, and bimolecular recombination on performance. Generation profiles calculated based on an optical transfer-matrix model (see **Figure 1b**) were used as input for the electrical device model, which thus accounts for interference effects. The default parameters in the simulations are listed in Table S1, Supporting Information, these parameters were used generally unless otherwise stated.

To check the validity of the model (including the experimentally determined parameters mentioned earlier) the J – V characteristics of devices with varying thickness were simulated and compared with experimentally measured ones. The J – V characteristics for a champion 100 nm thick inverted PM6:Y6 device is shown in **Figure 2a**, with $J_{SC} = 24.7 \text{ mA cm}^{-2}$, FF = 73.2%, and open circuit voltage $V_{OC} = 0.839 \text{ V}$ leading to a PCE of 15.2%. **Figure 2b,c** shows the J_{SC} , FF, and PCE of devices with varying thickness. The experimentally determined parameters are indicated by crosses (shown in Table S2, Supporting Information), and the result of the simulation is shown as a red line. For comparison, the maximum short-circuit current density $J_{SC,max}$, corresponding to the photocurrent expected when all photogenerated charge carriers are extracted (i.e., ideal charge generation and no recombination), is included in **Figure 2b** (blue dashed line). Device simulations and experimental data are, in general, in excellent agreement. Furthermore, it is clearly seen that the FF starts to drop significantly when the active layer thickness exceeds 100 nm. It should be noted that for these reference simulations, we assume no unintentional doping, as the doping concentrations are most likely highly device dependent. This could explain the small deviation at larger thicknesses, given that some doping was seen in thicker devices. In addition, also the optical constants, and thus the absorption coefficient, may vary slightly with increasing thickness, depending on how the morphology of the blend is affected by the processing conditions. Finally, it should be noted that the contacts are assumed nonselective, however, choosing selective contacts instead did not significantly change the results as seen in **Figure S6**, Supporting Information.

The charge carrier mobilities, doping concentrations, and recombination prefactor were next selectively varied in the simulations; the results are shown in **Figure 3**. The simulated J_{SC} , FF, and PCE as a function of active layers thickness in the inverted devices with varying p -doping concentration are shown

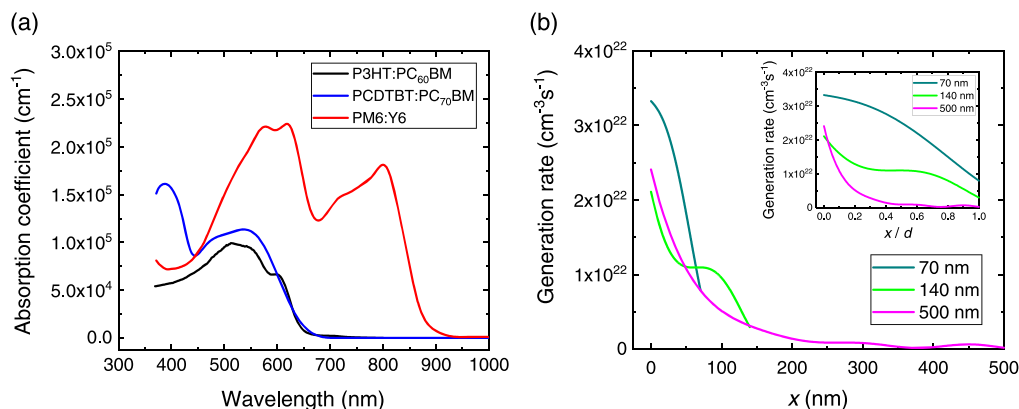


Figure 1. a) Absorption coefficients for P3HT:PC₆₀BM, PCDTBT:PC₇₀BM, and PM6:Y6 bulk-heterojunction blends. b) Generation profiles of devices with three different thicknesses are determined using an optical transfer-matrix model. The thickness of 70 nm is at the first interference maximum, whereas 140 nm is at the first interference minimum. Generation profiles vs the normalized device thickness are shown in the inset.

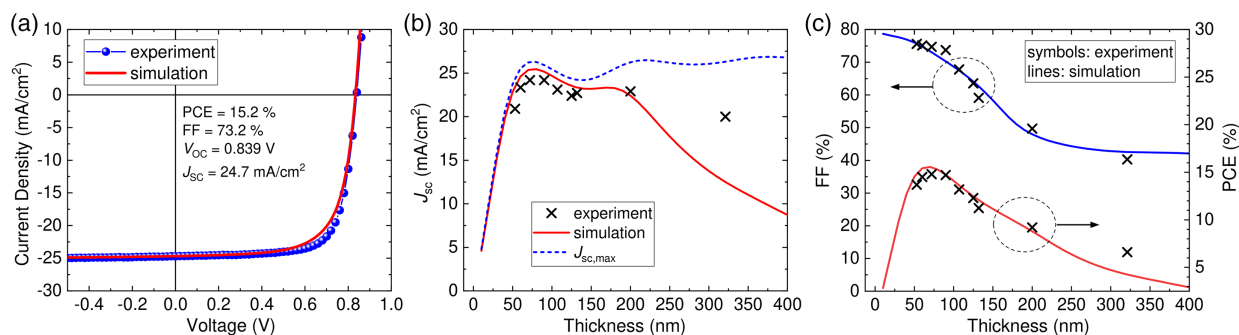


Figure 2. a) $J-V$ characteristic of a 100 nm-thick inverted PM6:Y6 device recorded under simulated AM 1.5G conditions (blue dots) and compared with DD simulations (red line). b) Experimentally determined short-circuit current density (black crosses) of PM6:Y6 devices plotted as a function of active layer thickness, and compared with DD simulations (red line) and the expected maximum short-circuit current (i.e., no recombination) based on the optical model (blue dashed line). c) Repetition of panel b), but instead of J_{sc} , the FF and PCE are plotted against the thickness of the active layer.

in Figure 3a–c. The red line indicates the reference (undoped) case and the measured values from Table S1, Supporting Information, are shown as black stars. It is clear that an increase in the doping concentrations leads to significantly improved device performance for active layer thicknesses exceeding

100 nm. The improved performance for increasing p -doping is related to the fact that in an inverted device structure, the depletion region forms at the transparent cathode. Charges generated in the depletion region are efficiently extracted as a significant part of the potential difference within the device drops over

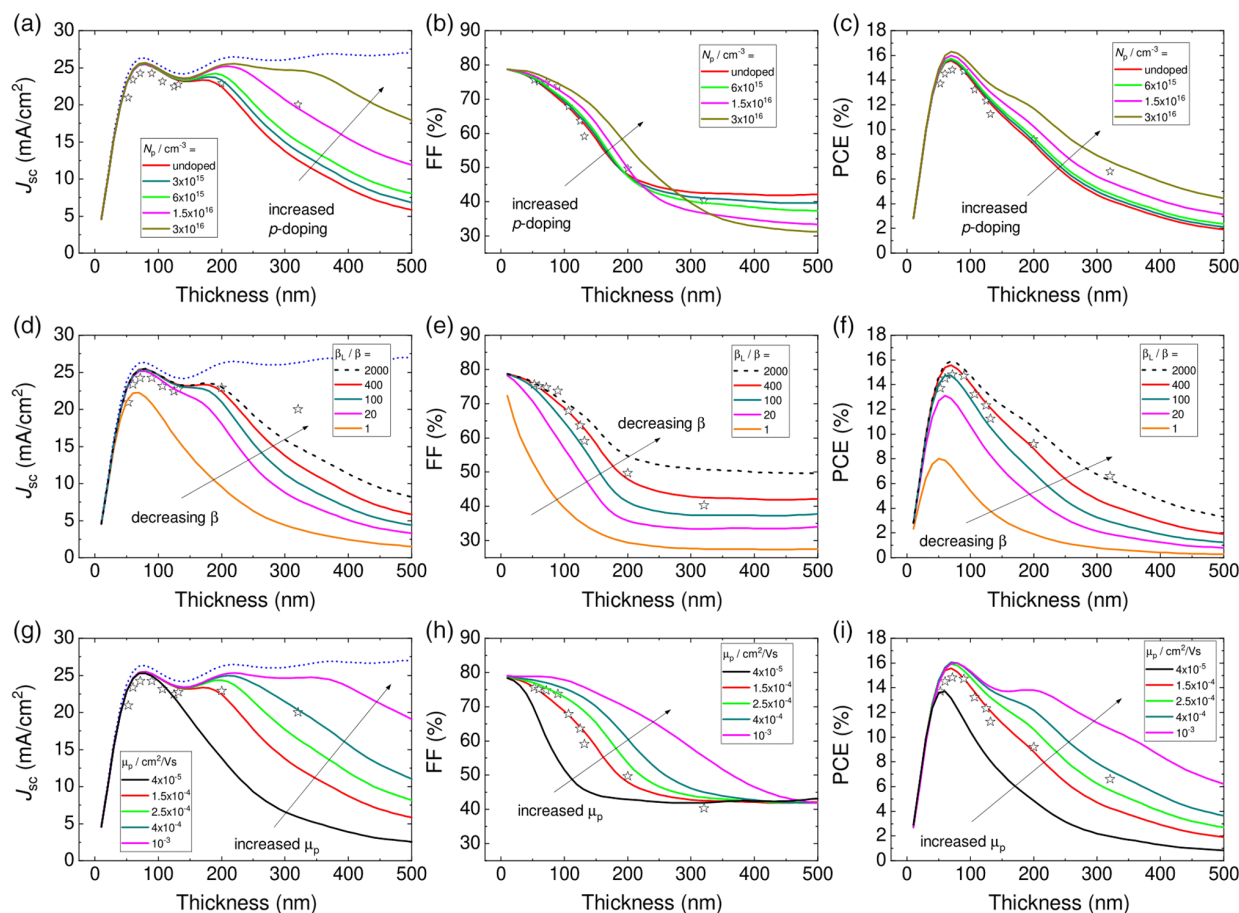


Figure 3. The effect on the photovoltaic parameters of a–c) p -doping the active layer (mobilities and recombination prefactor fixed), d–f) varying recombination prefactor (mobilities assumed fixed, no doping) and g–i) varying hole mobility (electron mobility and recombination prefactor fixed, no doping). The black open stars represent experimental values from Table S1, Supporting Information, and the blue dotted lines (panels a,d,g) are the maximum obtainable photocurrents (the case with no recombination).

the depletion region. The remaining neutral region effectively acts as an extension of the anode, which is beneficial for hole extraction given that holes have a longer distance to travel to the extracting contact than do electrons and the hole mobility is lower than the electron mobility. However, depending on the doping level and the conductivity of the majority carriers in the neutral region, a resistive potential drop may occur across this region as well.^[12] Furthermore, it should be noted that as the bimolecular recombination is ≈ 400 times reduced compared with the Langevin limit, charges generated in the neutral region can also diffuse out to the contacts and thereby contribute to the photocurrent. By *n*-doping the active layer the opposite effect is observed, i.e., device performance decreases for increasing doping concentration, as shown in Figure S7, Supporting Information. For a conventional structure device, the effect of doping would be the opposite, i.e., *p*-doping would be detrimental and *n*-doping beneficial for device performance, which partly explains the results by Lin et al.^[43] The fact that the simulations with *p*-doping agrees better with experiment than the simulations with *n*-doping, is a further indication that the unintentional doping observed in our doping-CELIV measurements was indeed of *p*-type.

The effect of varying bulk recombination on the device performance is shown in Figure 3d–f. As expected, increasing the reduction factor (lowering the bulk recombination rate) leads to improved performance over the whole thickness range. What is perhaps surprising, however, is that further increasing the reduction factor from the experimentally determined 400 to 2000 only improves performance by roughly 50%. This means that there is not much room for improvement, given that reduction factors exceeding 2000 are highly unlikely in organic BHJ blends.

The most dramatic effect on the performance of thick active layer devices is seen when the charge carrier mobility is varied, as shown in Figure 3g–i. Notably, at thicknesses exceeding 100 nm an increase in the hole mobility leads to clear improvements in performance, which is to be expected. What is surprising is that even minor increases in the mobility lead to significantly enhanced performance. For example, a reasonable increase in the hole mobility from the experimentally determined 1.5×10^{-4} to $10^{-3} \text{ cm}^2 \text{ Vs}^{-1}$ leads to an increase in PCE by roughly a factor of three at larger thicknesses. Furthermore, the PCE continues to improve even when the hole mobility becomes larger than the electron mobility, which is unexpected given that imbalanced charge carrier transport is typically expected to be detrimental for device performance. Figure S8, Supporting Information, where the electron mobility is varied, reinforces this point; a decrease in the electron mobility actually leads to an improved device performance at larger thicknesses.

The reason for this somewhat counterintuitive behavior is again related to the device structure and also to the absorption profile. In an inverted device structure where the charges are predominantly generated close to the transparent cathode, the hole transport becomes critical for device performance.^[11] In general, a lower hole mobility (compared with the electron one) leads to the formation of a space charge region in the vicinity of the anode which in turn leads to reduced FF and J_{SC} . This effect is accentuated in state-of-the-art NFA-based blends; the high absorption coefficients over a wide wavelength range leads to a sharper

absorption profile than in other BHJ blends where charge generation takes place further into the bulk. A sharp absorption profile also means that the performance of inverted devices does not suffer much from a low electron mobility, charges are generated so close to the cathode that electrons can be efficiently extracted even if the mobility is low. On the other hand, the holes need to traverse across the entire active layer. This imbalance in the charge extraction rates between the carrier types is compensated by a charge accumulation of holes, which screens the electric field within the active layer, ultimately reducing the overall charge collection. This is seen in the simulated band-diagrams shown in Figure 4. Note that the experimentally determined mobility imbalance ($\mu_n > \mu_p$) suggests that standard architecture devices would perform better than inverted ones at thick active layers, which is also shown in Figure S9, Supporting Information.

Thus far, one material property at a time has been varied showing that in the case of inverted NFA-based solar cells, *p*-doping of the active layer, increasing hole mobility and reducing the bimolecular recombination coefficient leads to improved performance, in particular at large thicknesses. These findings can be taken as general design rules for making thick junction NFA-based solar cells. We then varied several parameters simultaneously, to clarify the full potential of these design rules. Figure 5 shows heat maps of the PCE of devices with varying hole (*x*-axis) and electron (*y*-axis) mobilities. Figure 5a,b shows the case of 70 and 500 nm thick undoped active layers, respectively. For the 70 nm case, the best performance is obtained when the mobilities are more or less balanced, although increasing hole mobility seems to have a slightly more positive effect on performance than an increase in the electron mobility. For the 500 nm thick device, the situation is different, and an increase in PCE cannot be achieved unless the hole mobility is increased.

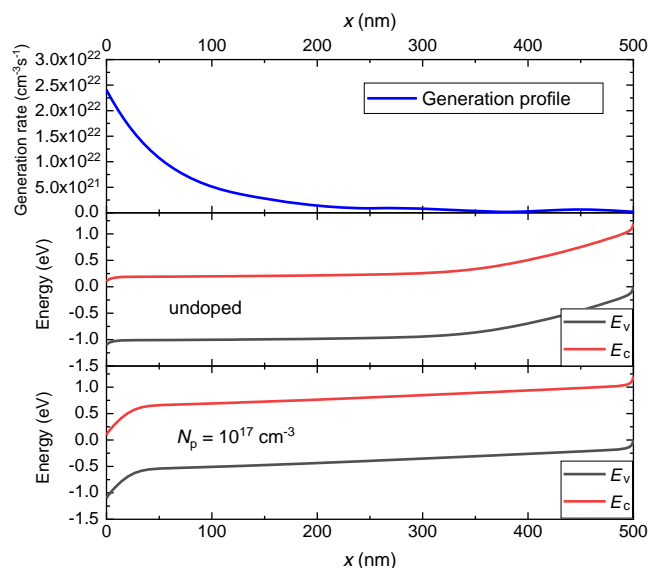


Figure 4. Simulated charge generation profile (upper panel) and band diagrams (valence band E_V in black and conduction band E_C in red) of an inverted PM6:Y6 solar cell (the middle panel is the undoped case and the lower panel is the case with a *p*-doping concentration of 10^{17} cm^{-3}).

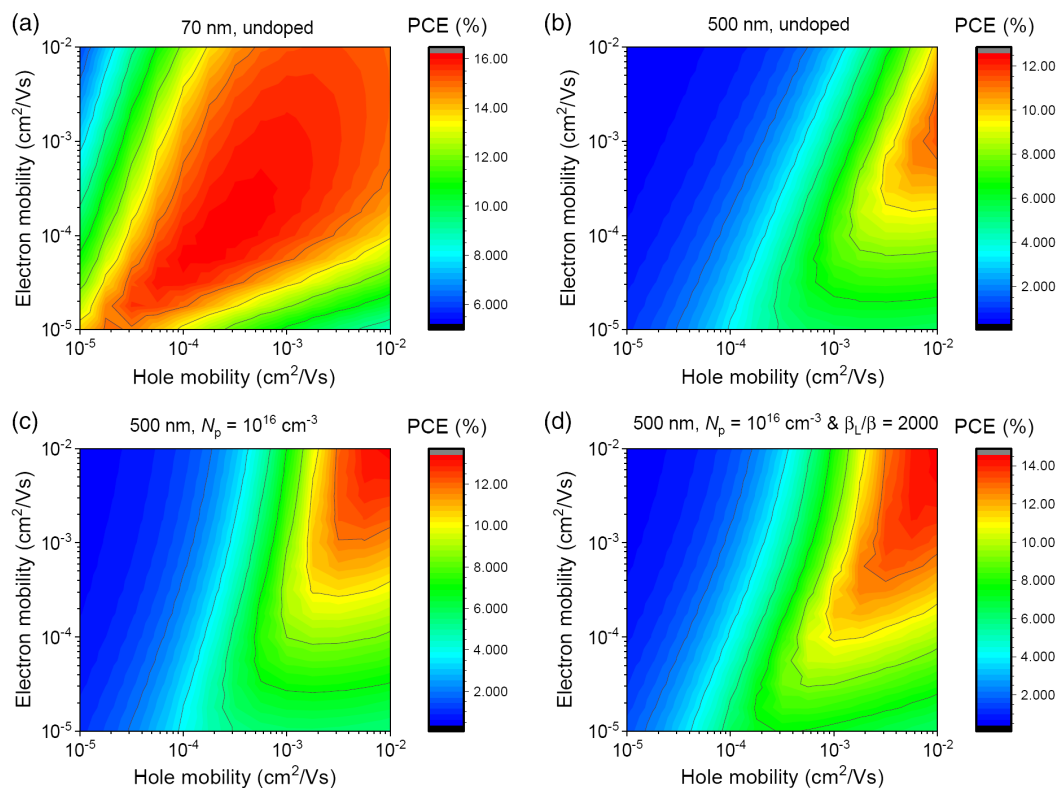


Figure 5. Heat maps of PCE as a function of electron and hole mobility for inverted NFA-based organic solar cells.

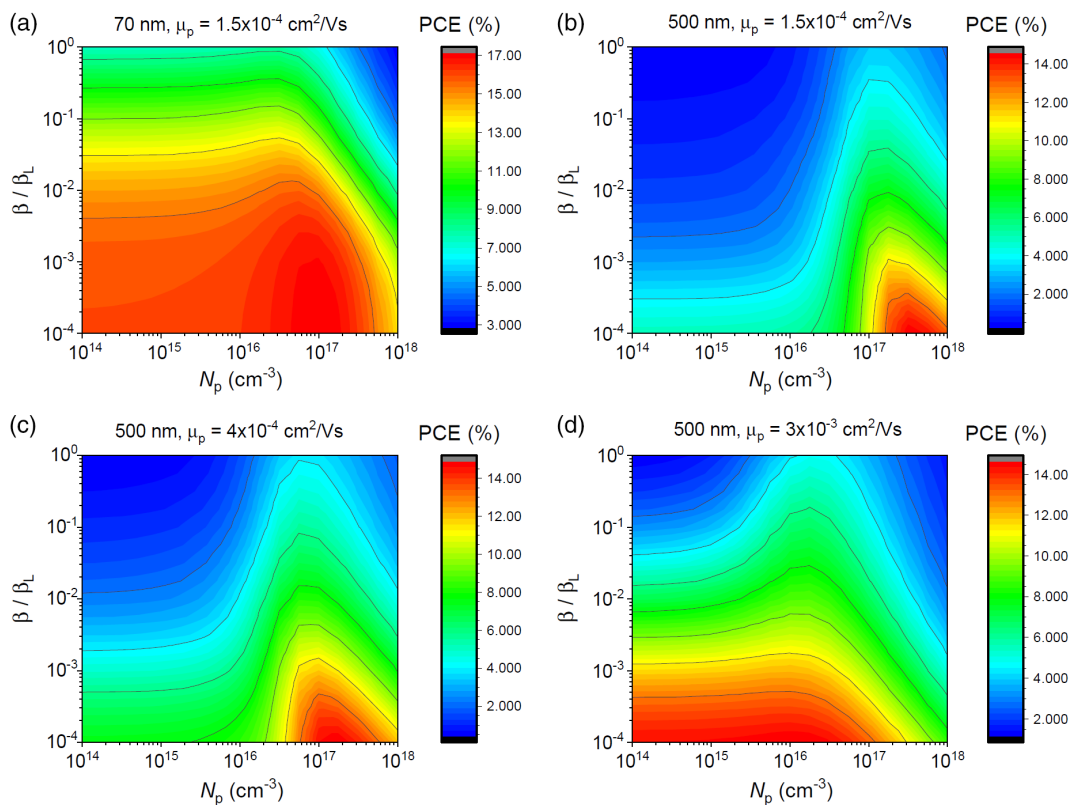


Figure 6. Heat maps of PCE as function of doping and bimolecular recombination for inverted NFA-based organic solar cells.

A similar trend is seen when the active layer is slightly *p*-doped (Figure 5c,d).

Figure 6 shows heat maps of the PCE of devices with varying doping concentration and recombination prefactor (β/β_L). Figure 6a shows the reference 70 nm device with mobilities taken from experiments. Figure 6b–d shows 500 nm thick devices with hole mobilities of 1.5×10^{-4} , 4×10^{-4} , and $3 \times 10^{-3} \text{ cm}^2 \text{ Vs}^{-1}$. Unsurprisingly, a reduction of the bimolecular recombination coefficient leads to improved performance in all cases. It has been shown that thick layers of Langevin-like systems ($\beta/\beta_L < 100$) suffer from CCN, i.e., only charges generated close to the transparent contact are efficiently extracted.^[11] This appears to be the case also here, however, what is shown in Figure 6 is that *p*-doping the active layer improves charge collection, especially in thick devices (Figure 6b–d) but also in the 70 nm case (Figure 5 and 6). The effect is largest for low hole mobilities, as expected, and if the mobility is high enough no doping is needed. What is furthermore seen is that there is an optimum doping concentration where the PCE is maximized, a lower or higher doping concentration leads to a decrease in PCE. The optimum doping concentration depends on the device thickness, carrier mobilities, and recombination coefficient, and cannot be readily described analytically. This highlights the importance of determining the doping concentration in NFA-based blends, in particular considering that it might be highly dependent on processing conditions and age of the device.

3. Conclusions

We have clarified the requirements for making NFA-based solar cells with thick active layers compatible with large-scale processing. We show that the most important factor limiting the performance of thick NFA-based solar cells is the collection of the charge carrier which is extracted opposite to the transparent contact (electrons when a conventional structure is used and holes in the case of an inverted structure). An increase in the conductivity of this charge carrier, either by increasing the carrier mobility or by doping, leads to significantly improved device performance. In NFA-based systems where the high absorption coefficients leads to sharp absorption profiles, the mobility of the charge carrier extracted at the transparent contact does not have to be high, in fact, lowering this mobility can actually lead to improved performance—there is a clear benefit from a mobility imbalance in this case. The effect of doping is more convoluted; there is an optimum doping concentration where performance is maximized, too much, or indeed, too little doping is detrimental. This highlights the importance of proper characterization of charge carrier mobilities (selectively for electrons and holes) and doping concentrations, especially as many systems are unintentionally doped. Furthermore, the fact that many organic semiconductors are prone to *p*-doping in the presence of oxygen suggests that an inverted structure might be more suitable for large-scale processing where contact with the ambient is difficult to avoid, even if the conventional structure makes better performing pristine devices. However, the complexity of the degradation processes and the multitude of possible sources for unintentional doping make it challenging to make general predictions and puts further emphasis on comprehensive characterization.

4. Experimental Section

Materials: PM6 and Y6 were purchased from Zhi-yan (Nanjing). 2,9-Bis[3-(dimethylamino)propyl]anthra[2,1,9-def:6,5,10-d'ef']diiisoquinoline-1,3,8,10(2H,9H)-tetrone (PDINO) was purchased from Solarmer. poly(3,4-ethylenedioxythiophene) polystyrene sulfonate (PEDOT:PSS) was obtained from Heraeus Deutschland GmbH (Clevios P VP.Al 4083).

Device Fabrication: PM6:Y6 solar cells were fabricated with an inverted architecture (glass/indium tin oxide (ITO)/ZnO/active layer/MoO₃/Ag). The commercial ITO-patterned glass electrodes were cleaned in detergent solution for 10 min followed by sonication in sequence in distilled water, acetone and 2-propanole each for 10 min. The cleaned substrates were dried with a stream of nitrogen and further treated with oxygen plasma. ZnO precursor solution was first prepared by dissolving 200 mg zinc acetate dihydrate in 2-methoxyethanol (2 mL) and ethanolamine (56 μL). The solution was stirred overnight under ambient condition and spin coated (4000 rpm for 30 s) on ITO substrate and further annealed at 200 °C for 1 h to make 30 nm ZnO film. PM6 and Y6 were dissolved in chloroform:1-chloronaphthalene (99.5:0.5, v/v) solution with the donor:acceptor ratio of 1:1.2 and spin coated on ZnO substrates. The thickness of PM6:Y6 active layers was adjusted by changing the concentration of the solution and the speed of spin coating. (16 mg mL⁻¹ solution with 3000 rpm for 53 nm, 16 mg mL⁻¹ solution with 2500 rpm for 60 nm, 16 mg mL⁻¹ solution with 2000 rpm for 72 nm, 16 mg mL⁻¹ solution with 1500 rpm for 90 nm, 30 mg mL⁻¹ solution with 8000 rpm for 107 nm, 30 mg mL⁻¹ solution with 6000 rpm for 125 nm, 30 mg mL⁻¹ solution with 4000 rpm for 132 nm, 30 mg mL⁻¹ solution with 2000 rpm for 200 nm, and 30 mg mL⁻¹ solution with 950 rpm for 321 nm). The as-cast PM6:Y6 films were then thermal annealed at 110 °C for 10 min. Afterward, 7 nm of MoO₃ and 100 nm of Ag were evaporated through a shadow mask in a vacuum chamber with <10⁻⁶ mbar base pressure. The thickness of ZnO and all active layer films were measured by a Dektak3ST profilometer.

MIS-CELIV: PM6:Y6 hole-only and electron-only MIS-CELIV devices were fabricated with an architecture of glass/ITO/PEDOT:PSS/active layer/Cytop/Ag and glass/ITO/PDINO/active layer/Cytop/Ag. For the hole-only device, a 40 nm PEDOT:PSS film was spin coated (6000 rpm) on precleaned ITO substrate and thermally annealed at 155 °C for 15 min. A 300 nm PM6:Y6 film was then spin coated (1200 rpm) onto the PEDOT:PSS from chloroform:1-chloronaphthalene (99.5:0.5, v/v) solution (30 mg mL⁻¹) and further thermal annealed at 110 °C for 10 min. Then 30 nm Cytop film was spin coated onto the active layer from the 10% CT = SOLV180 solution and thermally annealed at 60 °C for 30 min. Finally, 100 nm Ag was evaporated on the top of the Cytop as an anode. For the electron-only device, a 10 nm PDINO film was spin coated (3000 rpm) onto a precleaned ITO substrate from its methanol solution (1 mg mL⁻¹). A 250 nm PM6:Y6 film was then spin coated (1800 rpm) onto the PDINO from chloroform:1-chloronaphthalene (99.5:0.5, v/v) solution (30 mg mL⁻¹) and further thermally annealed at 110 °C for 10 min. Then a 30 nm Cytop film was spin coated onto the active layer from the 10% CT = SOLV180 solution and thermally annealed at 60 °C for 30 min. Finally, 100 nm Ag was evaporated on the top of the Cytop as a Cathode.

Basic Characterization: Absorption: The absorption of the PM6:Y6 blend was derived using a transmission spectrophotometry measurement (Perkin Elmer λ 950 equipped with 150 mm integrating sphere) on a 90 nm thick sample of PM6:Y6 on glass. A transmittance method script^[44] was used to determine the optical constants of the blend, from which the absorption coefficient α can be derived as:

$$\alpha = \frac{4\pi k}{\lambda} \quad (1)$$

k here being the imaginary component of the complex refractive index. In addition, ellipsometry was used in the Cauchy regime to verify the thickness of the sample.

Basic Characterization: Current–voltage (*J*–*V*) Measurements: Device *J*–*V* characterization was carried out under AM 1.5G (100 mW cm⁻²) using a Newport solar simulator (LCS-100) in air at room temperature. The light

intensity was calibrated using a standard silicon reference cell certified by the National Renewable Energy Laboratory (USA). J - V characteristics were recorded using J - V sweep software developed by Ossila Ltd. (UK). An aperture mask was placed over the devices to define the test area (2.40 mm²) and eliminate the influence of stray and wave guided light.

Charge Transport and Recombination Measurements: Resistance-dependent photovoltage: A Rhode & Schwarz Oscilloscope (RTM3004) and a variable load resistance varied between 50 Ω and 1 MΩ were used to record the RPV transients. Charge carriers in the active layer were photogenerated by a Pharos PH1-10 laser (20 Hz repetition rate, ≈290 fs pulse duration and 514 nm excitation wavelength) in combination with neutral optical density filters. The output power of the laser beam was set to less than 1 nJ cm⁻².

Charge Transport and Recombination Measurements: CELIV: A waveform function generation from Keysight (33500B series) was used to generate a charge extraction by linearly increasing voltage (CELIV) triangle pulse. Time delay and voltage slope were adjusted with the function generator. A Rhode & Schwarz Oscilloscope (RTM3004) with an input load resistance of 50 Ω was used to record the CELIV signal. The variable load resistance VT2 from Thorlabs providing variable resistances between 50 Ω and 100 kΩ was put in series with the external circuit, respectively, in parallel with the Oscilloscope.

Charge Transport and Recombination Measurements: Double-Injection: A Keysight 33500B waveform function generator with variable voltage and time delay was used to apply a square voltage pulse on the device. The current signal was recorded using a Rhode & Schwarz Oscilloscope (RTM3004). Steady-state current signals were measured using a Keithley 2450 source measure unit (SMU) by applying variable forward bias voltages directly on the device under test (DUT).

Device Model: A combined electro-optical device model has been used for the simulations. The electrical transport is described using a numerical 1D DD model, assuming the bulk heterojunction to behave as an effective semiconductor active layer with effective energy levels.^[42] The numerical model solves the charge carrier continuity equations for the electron (n) and hole (p) density, in conjunction with the Poisson equation for the electrical potential, and assuming the electron and hole currents to be governed by DD. A numerical approach based on the Scharfetter–Gummel discretization scheme of the current equations and Gummel's iteration method for the potential is used.^[45–47] The carrier densities are assumed to be at thermal equilibrium in the active layer at the anode and cathode interfaces, implying nonselective (sink) contacts with respect to charge carrier extraction. The charge transport in the active layer is described using effective mobilities, μ_n and μ_p , for electrons in the acceptor phase and holes in the donor phase, respectively. The recombination rate between electrons and holes in the active layer is assumed to be bimolecular, given by $R = \beta np$, having a recombination coefficient given by $\beta = \zeta \beta_L$, where ζ is the Langevin reduction factor and $\beta_L = q[\mu_n + \mu_p]/\epsilon\epsilon_0$ with q being the elementary charge, ϵ the relative permittivity of the active layer, and ϵ_0 is the vacuum permittivity. Finally, the generation rate profile for charge carriers inside the active layer is calculated using an optical transfer-matrix model.^[40,41] An incident light intensity following the AM1.5 G solar spectrum is assumed. Based on the refractive indices and extinction coefficients of the different layers constituting the device stack (glass, electrodes, interlayers, active layer), the transfer-matrix model then evaluates the optical field inside the active layer considering wavelength-dependent absorption, reflection, and interference effects. For simplicity, we assume that all absorbed photons are converted into free electron–hole pairs.

MIS-CELIV: For MIS-CELIV, a metal/semiconductor/insulator/metal device structure was used, constituting an active semiconductor layer sandwiched between an injecting top (metal) electrode and a thin charge-carrier blocking insulator layer (on the bottom electrode).^[32,33] A large applied prebias voltage was used to inject carriers from the injecting contact to form an injected charge-carrier reservoir in the active layer at the insulator interface. By subsequently applying a linearly increasing voltage pulse of opposite polarity, this charge reservoir was extracted at the top contact allowing for the charge transport properties to be probed. The associated time-dependent extraction current density is given by

$$j(t) = \Delta j(t) + j_0^* \quad (2)$$

being composed of the time-dependent average conduction current $\Delta j(t)$ and the constant average displacement current $j_0^* = \frac{\epsilon\epsilon_0 A}{d}$ across the device. Here, $A^* = \frac{A}{1+f}$ and $f = \frac{\epsilon d}{\epsilon_i d_i}$, where A is the voltage ramp-up rate, ϵ_0 is the vacuum permittivity, whereas ϵ (ϵ_i) and d (d_i) are the relative permittivity and thicknesses of the active semiconductor layer (insulator layer), respectively. In the space-charge-limited current extraction regime, the mobility can be determined from the time t_1 at which $j(t_1) = 2j_0^*$ via

$$\mu = \frac{\pi^2 d^2}{8A^* t_1^2} (1+f) \quad (3)$$

However, this expression is only valid for large $A^* t_1$.^[33] In the case of an undoped active layer with an ohmic injecting contact, the ohmic extraction current regime, induced by carriers diffused into the active layer from this contact, needs to be considered; under these conditions the mobility may be estimated using^[33]

$$\mu = \frac{\pi^2 d^2}{8A^* t_1^2} \frac{(1+f)}{\left[1 + \frac{\pi^2 kT}{2qA^* t_1}\right]} \quad (4)$$

for $A^* t_1 \gg kT/q$, where kT/q is the thermal voltage. On the other hand, in case of a p -doped device, the extraction current transient is instead dominated by an ohmic extraction current regime induced by the doping-induced hole conductivity of the active layer. In this limit, the initial hole extraction current density is given by^[48]

$$j(t) = j_0^* \left[\frac{t}{\tau_\sigma} + 1 \right] \quad (5)$$

where $\tau_\sigma = \frac{\epsilon\epsilon_0}{qN_p\mu_p}$ is the dielectric relaxation time, with N_p being the doping concentration of holes and q the elementary charge; hence, in this case, the hole mobility is obtained using from

$$\mu_p = \frac{\epsilon\epsilon_0}{qN_p t_1} \quad (6)$$

when $A^* t_1 \ll \frac{\pi^2 q N_p d^2}{8\epsilon\epsilon_0}$.

Double-Injection: To estimate the recombination prefactor ζ , double-injection (DoI) measurements were carried out in the dark. In DoI, the injection current of a diode device with two ohmic contacts was measured at large forward bias voltages, greater than the built-in voltage V_{bi} . Under these conditions, the dark steady-state current, being composed of an electron current (injected from the anode) and a hole current (injected from the cathode), is limited by both recombination and space charge of electrons and holes in the active layer. Under conditions when $\beta < \beta_L$, corresponding to the injected electron–hole plasma limit, the (saturated) double-injection current density can be approximated by^[36–38]

$$J_{DOI} = \frac{9}{8} \sqrt{\frac{16\pi\beta_L}{9\beta} \mu_n \mu_p \epsilon\epsilon_0} \frac{(V - V_{bi})^2}{d^3} \quad (7)$$

where V is the voltage across the active layer and d is the active layer thickness. Accordingly, provided that the mobilities are known, the Langevin reduction factor $\zeta = \beta/\beta_L$ can be determined from J_{DOI} via

$$\frac{\beta_L}{\beta} = \frac{9}{16\pi} \frac{(\mu_n + \mu_p)^2}{\mu_n \mu_p} \left(\frac{J_{DOI}}{J_{SCLC}} \right)^2 \quad (8)$$

where

$$J_{SCLC} = \frac{9}{8} \epsilon\epsilon_0 [\mu_n + \mu_p] \frac{(V - V_{bi})^2}{d^3} \quad (9)$$

Finally, it is important to note that because the DoI current densities are often large (especially in thin-film devices), corresponding to high-

injection conditions, a non-negligible voltage drop will generally occur in the external circuit (including the electrodes and the wires) owing to its finite series resistance. Accounting for this resistive voltage loss, the voltage across the active layer is given by

$$V = V_{\text{appl}} - R_s J_{\text{DOI}} \quad (10)$$

where V_{appl} is the externally applied voltage and R_s is the total series resistance (in units of Ωcm^2) of the external circuit.

Supporting Information

Supporting Information is available from the Wiley Online Library or from the author.

Acknowledgements

M.N. and O.J.S. contributed equally to this work. M.N. acknowledges funding from the Academy of Finland through project #326000. This work was also funded by the Welsh Government's Sêr Cymru II Program through the European Regional Development Fund and Welsh European Funding Office. S.Z. and R.K. are recipients of UKRI EPSRC Doctoral Training Program studentships. P.M. is a Sêr Cymru II Research Chair and A.A. a Rising Star Fellow also funded by the Welsh Government's Sêr Cymru II Program through the European Regional Development Fund, Welsh European Funding Office and Swansea University Strategic Initiative in Sustainable Advanced Materials. Prof. R. Österbacka is acknowledged for fruitful discussions.

Conflict of Interest

The authors declare no conflict of interest.

Data Availability Statement

Data available on request from the authors.

Keywords

charge carrier mobilities, doping, nonfullerene acceptors, organic photovoltaics, recombination

Received: January 8, 2021

Revised: February 3, 2021

Published online: March 3, 2021

- [1] J. Hou, O. Inganäs, R. Friend, F. Gao, *Nat. Mater.* **2018**, *17*, 119.
- [2] NREL, *Research Cell Efficiency Record*, <https://www.nrel.gov/pv/assets/pdfs/best-research-cell-efficiencies.20200406.pdf> (accessed: May 2020).
- [3] N. Bauer, Q. Zhang, J. Zhao, L. Ye, J.-H. Kim, I. Constantinou, L. Yan, F. So, H. Ade, H. Yan, W. You, *J. Mater. Chem. A* **2017**, *5*, 4886.
- [4] X. Zhang, X. Zuo, S. Xie, J. Yuan, H. Zhou, Y. Zhang, *J. Mater. Chem. A* **2017**, *5*, 17230.
- [5] B. Xiao, J. Song, B. Guo, M. Zhang, W. Li, R. Zhou, J. Liu, H.-B. Wang, G. Luo, F. Liu, T. P. Russel, *J. Mater. Chem. A* **2018**, *6*, 957.
- [6] Y. Firdaus, V. M. Le Corre, J. I. Khan, Z. Kan, F. Laquai, P. M. Beaujuge, T. D. Anthopoulos, *Adv. Sci.* **2019**, *6*, 1802028.
- [7] T. Kirchartz, T. Agostinelli, M. Campoy-Quiles, W. Gong, J. Nelson, *Phys. Chem. Lett.* **2012**, *3*, 3470.
- [8] P. Meredith, A. Armin, *Nat. Commun.* **2018**, *9*, 5261.
- [9] S. Wilken, O. J. Sandberg, D. Scheunemann, R. Österbacka, *Sol. RRL* **2020**, *4*, 1900505.
- [10] J. A. Bartelt, D. Lam, T. M. Burke, S. M. Sweetnam, M. D. McGehee, *Adv. Energy Mater.* **2015**, *5*, 1500577.
- [11] A. Armin, A. Yazmaciyan, M. Hamsch, J. Li, P. L. Burn, P. Meredith, *ACS Photonics* **2015**, *2*, 1745.
- [12] O. J. Sandberg, S. Dahlström, M. Nyman, S. Wilken, D. Scheunemann, R. Österbacka, *Phys. Rev. Applied* **2019**, *12*, 034008.
- [13] A. Seemann, T. Sauermann, C. Lungenschmied, O. Armbruster, S. Bauer, H.-J. Egelhaaf, J. Hauch, *Solar Energy* **2011**, *85*, 1238.
- [14] J. Schafferhans, A. Baumann, A. Wagenpfahl, C. Deibel, V. Dyakonov, *Org. Electron.* **2010**, *11*, 1693.
- [15] M. L. Tietze, K. Leo, B. Lüssem, *Org. Electron.* **2013**, *14*, 2348.
- [16] A. J. Morfa, A. M. Nardes, S. E. Shaheen, N. Kopidakis, J. van de Lagemaat, *Adv. Funct. Mater.* **2011**, *21*, 2580.
- [17] M. Nyman, S. Dahlström, O. J. Sandberg, R. Österbacka, *Adv. Energy Mater.* **2016**, *6*, 1600670.
- [18] F. Deledalle, T. Kirchartz, M. S. Vezie, M. Campoy-Quiles, P. S. Tuladhar, J. Nelson, and J. R. Durrant, *Phys. Rev. X* **2015**, *5*, 011032.
- [19] A. Pivrikas, G. Juška, A. J. Mozer, M. Scharber, K. Arlauskas, N. S. Sariciftci, H. Stubb, R. Österbacka, *Phys. Rev. Lett.* **2005**, *94*, 176806.
- [20] T. M. Clarke, D. B. Rodovsky, A. A. Herzing, J. Peet, G. Dennler, D. DeLongchamp, C. Lungenschmied, A. J. Mozer, *Adv. Energy Mater.* **2011**, *1*, 1062.
- [21] Y. Jin, Z. Chen, S. Dong, N. Zheng, L. Ying, X.-F. Jiang, F. Liu, F. Huang, Y. Cao, *Adv. Mater.* **2016**, *28*, 9811.
- [22] K. N. Schwarz, P. B. Geraghty, V. D. Mitchell, S.-U.-Z. Khan, O. J. Sandberg, N. Zarrabi, B. Kudisch, J. Subbiah, T. A. Smith, B. P. Rand, A. Armin, G. D. Scholes, D. J. Jones, K. P. Ghiggino, *J. Am. Chem. Soc.* **2020**, *142*, 2562.
- [23] N. Tokmoldin, S. M. Hosseini, M. Raoufi, L. Q. Phuong, O. J. Sandberg, H. Guan, Y. Zou, D. Neher, S. Shoaee, *J. Mater. Chem. A* **2020**, *8*, 7854.
- [24] J. Yuan, Y. Zhang, L. Zhou, G. Zhang, T.-K. Lau, X. Lu, H. Peng, Y. Li, P. A. Johnson, M. Leclerc, H.-L. Yip, Y. Cao, J. Ulanski, Y. Zou, *Joule* **2019**, *3*, 1140.
- [25] S. M. Hosseini, N. Tokmoldin, Y. W. Lee, Y. Zou, H. Y. Woo, D. Neher, S. Shoaee, *Sol. RRL* **2020**, *4*, 2000498.
- [26] L. Ma, S. Zhang, H. Yao, Y. Xu, J. Wang, Y. Zu, J. Hou, *ACS Appl. Mater. Interfaces* **2020**, *12*, 18777.
- [27] L. Ma, Y. Xu, Y. Zu, Q. Liao, B. Xu, C. An, S. Zhang, J. Hou, *Sci. China Chem.* **2020**, *63*, 21.
- [28] A. Melianas, M. Kemerink, *Adv. Mater.* **2019**, *31*, 1806004.
- [29] B. Philippa, M. Stolterfoht, P. L. Burn, G. Juška, P. Meredith, R. D. White, A. Pivrikas, *Sci. Rep.* **2014**, *4*, 5695.
- [30] S. Dahlström, O. J. Sandberg, M. Nyman, R. Österbacka, *Phys. Rev. Appl.* **2018**, *10*, 054019.
- [31] S. Dahlström, C. Ahläng, K. Björkström, S. Forsblom, B. Granroth, K. Jansson, A. Luukkonen, M. T. Masood, J. Poulizac, S. Qudsia, M. Nyman, *AIP Adv.* **2020**, *10*, 065203.
- [32] G. Juška, N. Nekrašas, K. Genevičius, *J. Non-Crystall. Solids* **2012**, *358*, 748.
- [33] O. J. Sandberg, M. Nyman, S. Dahlström, S. Sandén, B. Törngren, J.-H. Smätt, R. Österbacka, *Appl. Phys. Lett.* **2017**, *110*, 153504.
- [34] O. J. Sandberg, M. Nyman, R. Österbacka, *Org. Electron.* **2014**, *15*, 3413.
- [35] M. Nyman, O. J. Sandberg, S. Dahlström, D. Spoltore, C. Körner, Y. Zhang, S. Barlow, S. R. Marder, K. Leo, K. Vandewal, R. Österbacka, *Sci. Rep.* **2017**, *7*, 5397.

- [36] M. A. Lampert, P. Mark, *Current Injection in Solids*, Academic Press, New York **1970**.
- [37] A. Pivrikas, N. S. Sariciftci, G. Juška, R. Österbacka, *Prog. Photovolt: Res. Appl.* **2007**, *15*, 677.
- [38] G. A. H. Wetzelaer, N. J. Van der Kaap, L. J. A. Koster, P. W. M. Blom, *Adv. Energy Mater.* **2013**, *3*, 1130.
- [39] A. Sundqvist, O. J. Sandberg, M. Nyman, J.-H. Smått, R. Österbacka, *Adv. Energy Mater.* **2016**, *6*, 1502265.
- [40] L. A. Pettersson, L. S. Roman, O. Inganäs, *J. Appl. Phys.* **1999**, *86*, 487.
- [41] G. F. Burkhard, E. T. Hoke, M. D. McGehee, *Adv. Mater.* **2010**, *22*, 3293.
- [42] O. J. Sandberg, A. Sundqvist, M. Nyman & R. Österbacka *Phys. Rev. Appl.* **2016**, *5*, 044005.
- [43] Y. Lin, Y. Firdaus, M. I. Nugraha, F. Liu, S. Karuthedath, A.-H. Emwas, W. Zhang, A. Seitkhan, M. Neophytou, H. Faber, E. Yengel, I. McCulloch, L. Tsetseris, F. Laquai, T. D. Anthopoulos, *Adv. Sci.* **2020**, *7*, 1903419.
- [44] R. Kerremans, C. Kaiser, W. Li, N. Zarrabi, P. Meredith, A. Armin, *Adv. Opt. Mater.* **2020**, 2000319, 2195.
- [45] H. K. Gummel, *IEEE Trans. Electron Devices* **1964**, *11*, 455.
- [46] D. L. Scharfetter, H. K. Gummel, *IEEE Trans. Electron Devices* **1969**, *16*, 64.
- [47] S. Selberherr, *Analysis and Simulation of Semiconductor Devices*, Springer-Verlag, Wien **1984**.
- [48] G. Juška, K. Arlauskas, M. Viliūnas, J. Kočka, *Phys. Rev. Lett.* **2000**, *84*, 4946.